longitudes; in panels B and C, obtained just 6 days apart, the ring appears to be consistently brightest at longitudes leading (to the right of) Portia, which can be identified in the figure as R2's bright interior neighbor. If R2 arises from a belt of macroscopic bodies, then the brighter clumps might be transient phenomena arising when embedded parent bodies collide; a similar process is believed to be at work in Saturn's clumpy F ring (*18*–*21*).

Discussion. Dynamical simulations of the closely packed inner uranian moons reveal that they will perturb each other into crossing orbits at million-year time scales (*3*). The discovery of Cupid orbiting so close to Belinda substantially exacerbates the stability problem (*22*). Our new findings provide a clearer picture of this rapidly and chaotically evolving system. The largest moons show orbital changes within decades; these subtle variations can, over time, lead to orbital collisions and disruptions. So close to the Roche limit, one might expect to find one or more debris belts within this evolving system; R2 is likely to be one such example. Mab and R1 are distant enough to be unaffected by the dynamical turmoil within the Portia group, but the mysterious orbital variations of Mab suggest that it may play a part in the underlying interactions. It is as yet unclear whether related phenomena are at work within Uranus's main ring system.

The rings and smaller moons listed in Tables 1 and 2 have probably changed quite substantially since the time of the dinosaurs, and perhaps even since the time of the Roman Empire. Uranus does not host a swarm of independent moons and rings, but instead features a closely coupled dynamical system that rivals the other known ring-moon systems in its subtlety and complexity.

References and Notes

1. B. A. Smith *et al.*, *Science* **233**, 43 (1986).
2. E. Karkoschka, *Icarus* **151**, 69 (2001).
3. M. J. Duncan, J. J. Lissauer, *Icarus* **125**, 1 (1997).
4. See supporting material on *Science* Online.
5. M. R. Showalter, J. J. Lissauer, *IAU Circ. 8194* (2003).
6. M. R. Showalter, J. J. Lissauer, *IAU Circ. 8209* (2003).
7. E. Karkoschka, *Icarus* **151**, 51 (2001).
8. W. M. Owen Jr., S. P. Synnott, *Astron. J.* **93**, 1268 (1987).
9. R. A. Jacobson, *Astron. J.* **115**, 1195 (1998).
10. J. A. Burns, D. P. Hamilton, M. R. Showalter, in *Interplanetary Dust*, E. Grün, B. A. S. Gustafson, S. F. Dermott, H. Fechtig, Eds. (Springer-Verlag, Berlin, 2001), pp. 641–725.
11. J. A. Burns et al., in *Jupiter: The Planet, Satellites and Magnetosphere*, F. Bagenal, Ed. (Cambridge Univ. Press, Cambridge, 2004), pp. 241–262.
12. M. R. Showalter, J. N. Cuzzi, *Icarus* **103**, 124 (1993).
13. H. B. Throop, L. W. Esposito, *Icarus* **131**, 152 (1998).
14. J. J. Lissauer, R. G. French, *Icarus* **146**, 12 (2000).
15. A. L. Broadfoot *et al.*, *Science* **233**, 74 (1986).
16. J. E. Colwell, L. W. Esposito, *Icarus* **86**, 530 (1990).
17. J. E. Colwell, L. W. Esposito, *J. Geophys. Res.* **97**, 10227 (1992).
18. J. N. Cuzzi, J. A. Burns, *Icarus* **74**, 284 (1988).
19. M. R. Showalter, *Science* **282**, 1099 (1998).
20. F. Poulet, B. Sicardy, P. D. Nicholson, E. Karkoschka, J. Caldwell, *Icarus* **144**, 135 (2000).
21. J. M. Barbara, L. W. Esposito, *Icarus* **160**, 161 (2002).
22. J. A. Meyer, personal communication.

23. Support for this publication was provided by NASA through proposals GO-9823, GO-10102, and GO-10274 from the Space Telescope Science Institute, which is operated by the Association of Universities for Research in Astronomy under NASA contract NAS5-26555. Additional support was provided by NASA's Planetary Geology and Geophysics Program (M.R.S.). We thank A. Roman and R. Gilliland for their extensive support in the planning and execution of our HST observations.

Supporting Online Material

www.sciencemag.org/cgi/content/full/1122882/DC1
Materials and Methods
Tables S1 to S3
Movie S1

21 November 2005; accepted 15 December 2005
Published online 22 December 2005;
10.1126/science.1122882
Include this information when citing this paper.

REPORTS

Electrodes with High Power and High Capacity for Rechargeable Lithium Batteries

Kisuk Kang,[1] Ying Shirley Meng,[1] Julien Bréger,[2] Clare P. Grey,[2] Gerbrand Ceder[1]*

New applications such as hybrid electric vehicles and power backup require rechargeable batteries that combine high energy density with high charge and discharge rate capability. Using ab initio computational modeling, we identified useful strategies to design higher rate battery electrodes and tested them on lithium nickel manganese oxide [$Li(Ni_{0.5}Mn_{0.5})O_2$], a safe, inexpensive material that has been thought to have poor intrinsic rate capability. By modifying its crystal structure, we obtained unexpectedly high rate-capability, considerably better than lithium cobalt oxide ($LiCoO_2$), the current battery electrode material of choice.

Rechargeable Li batteries offer the highest energy density of any battery technology, and they power most of today's portable electronics. Although most electronics require only moderately high charge/discharge rates, newer applications, such as regenerative braking in hybrid electric vehicles (HEVs), power backup, and portable power tools, require both high energy and high power density (i.e., the ability to charge and discharge very fast), which has been difficult to accomplish with Li batteries. Cathode electrodes in rechargeable Li batteries store Li^+ and electrons by the concurrent insertion of Li^+ in a crystal structure and the reduction of a transition-metal ion (*1*). Good electrode materials therefore have high reversible storage capacity for Li (to obtain long battery life per unit weight or volume of the battery) and rapid solid-state Li^+ and electron transport. Reasonable charge/discharge times require that, at room temperature, Li^+ ions can diffuse over micrometer distances in a matter of an hour (minutes for HEV technology). Hence, materials with very fast Li diffusivity are needed to produce batteries capable of satisfying high power demands in new applications. In this report, we use ab initio computational modeling to identify the basic energy barrier that limits Li^+-ion hopping in a prototypical layered electrode structure and use the insights gained from these calculations to synthesize a material with substantially better rate capability.

Many current (e.g., $LiCoO_2$ in today's batteries) and potential intercalation electrodes have the layered structure shown in Fig. 1A, consisting of layers of transition-metal cations separated from Li layers by oxygen. In this structure, Li is coordinated octahedrally by oxygens but diffuses from site to site by hopping through intermediate tetrahedral sites (Fig. 1B) (*2*). Previous work has identified the tetrahedral site as being close to the maximum-energy position along the path between octahedral sites (*3*). Because Li hops require thermal energy fluctuations, the hopping rate decreases exponentially with the energy of the activated state, and small reductions in this activation energy can lead to substantial improvement of the Li diffusion and of the rate at which an electrode can be charged or discharged. At room temperature, a reduction of activation energy of only 57 meV increases the rate of Li migration by a factor of 10 [$\exp(-57\ meV/kT) \sim 10$]. The energy required for a Li^+ ion to cross the activated

[1]Center for Materials Science and Engineering and Department of Materials Science and Engineering, Massachusetts Institute of Technology, 77 Massachusetts Avenue, Cambridge, MA 02139, USA. [2]Department of Chemistry, State University of New York, Stony Brook, NY 11794–3400, USA.

*To whom correspondence should be addressed. E-mail: gceder@mit.edu

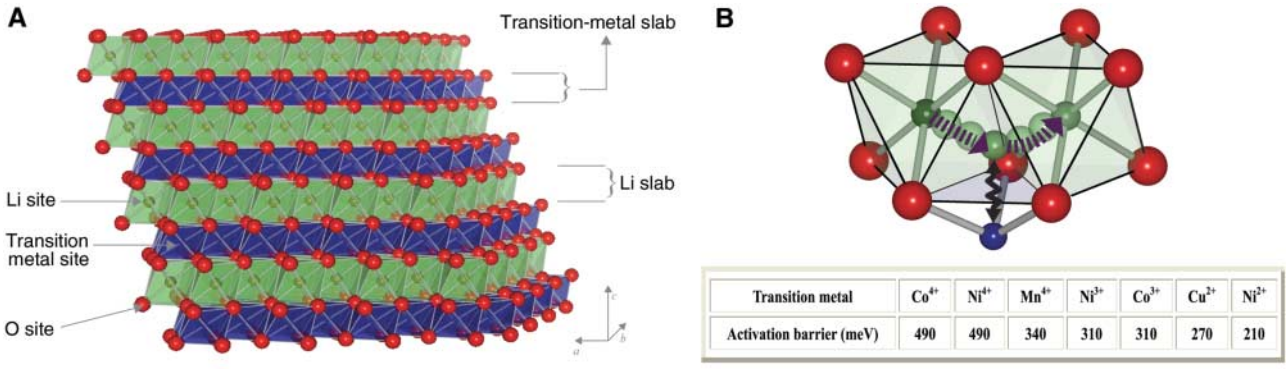

Transition metal	Co^{4+}	Ni^{4+}	Mn^{4+}	Ni^{3+}	Co^{3+}	Cu^{2+}	Ni^{2+}
Activation barrier (meV)	490	490	340	310	310	270	210

Fig. 1. (**A**) The structure of $Li(Ni_{0.5}Mn_{0.5})O_2$ consists of layers of transition metal (Ni and Mn) separated from Li layers by oxygen. In materials made by a conventional high-temperature synthesis, partial exchange of Li and Ni ions is always observed, which contracts the space through which Li can move. (**B**) Li moves from one octahedral site to another by passing through an intermediate tetrahedral site where it encounters strong repulsion from a nearby transition-metal cation. The table shows the activation barrier for Li motion for various transition metals near the activated state. Values were calculated by GGA DFT for various chemistries and Li contents.

state is likely to depend on the size of the tetrahedral site (strain effect) as well as on the electrostatic interaction between Li^+ in the activated state and the transition-metal cation directly below it (Fig. 1B). Hence, a strategy to increase Li diffusivity should focus on reducing these two contributions to the activation energy.

Using ab initio calculations performed in the generalized gradient approximation to density functional theory (GGA DFT), we can gauge the effect of both the strain and electrostatic contributions to the activation energy. The table in Fig. 1B shows the calculated energy for a Li^+ ion in the tetrahedral site with various other cations in the face-sharing octahedron adjoining it. Clearly, a low-valent transition metal such as Ni^{2+} is beneficial to the Li diffusion. The reduction from Co^{3+} (currently used) to Ni^{2+} leads to a hopping rate that is higher by a factor of 54 [$\sim\exp(100\ meV/kT)$]. Hence, a material such as $Li(Ni^{2+}_{0.5}Mn^{4+}_{0.5})O_2$, in which half the Li^+-activated states come in contact with Ni^{2+}, should have substantially higher Li diffusivity at the early stage of charging than the currently used battery material $LiCoO_2$, in which all the pathways are in contact with Co^{3+}. Because the number of high-rate pathways is well above the percolation limit, the presence of low-rate pathways (in contact with Mn^{4+}) in $LiNi_{0.5}Mn_{0.5}O_2$ should not substantially reduce the Li diffusivity. It is expected that the benefit of Ni^{2+} is noticeable until the charging level is so high that the Ni^{2+} pathways do not percolate anymore.

$LiNi_{0.5}Mn_{0.5}O_2$ is fundamentally different from the currently used electrode material, $LiCoO_2$, in which Co can only exchange one electron, and removal of all Li leads to an unstable material containing only highly oxidized Co^{4+} ions. In comparison, the transition-metal layer in $Li(Ni_{0.5}Mn_{0.5})O_2$ is bifunctional, with Ni^{2+} acting as a double redox-active center (*4*–*7*) and Mn^{4+} providing stability to the host structure (*8*). Although the distinctive electronic properties of $Li(Ni_{0.5}Mn_{0.5})O_2$ have been shown to result in high battery capacity for this material at very low charge/discharge rates (*4*, *5*, *9*, *10*), this capacity advantage over current electrode materials completely disappears at commercially interesting rates, in apparent contradiction to the predictions made based on the calculations (Fig. 1B). Our calculations were performed for materials with an ideal layered structure. However, in all $Li(Ni_{0.5}Mn_{0.5})O_2$ materials synthesized thus far, perfect separation between Li and transition-metal cations into alternating layers could not be achieved, with all materials exhibiting 8 to 12% exchange of Li and Ni (*4*, *5*, *9*, *10*). Calculations were, therefore, performed to explore the effect of Li/Ni site exchange on the Li mobility. Figure 2 shows ab initio computations of the activation energy as a function of the distance between the oxygen layers on each side of the plane of Li^+ ions (Fig. 2). As this layer-to-layer distance grows, the space in the activation site increases. It is clear that more space between these oxygen layers substantially reduces the activation energy for Li motion. These calculations also clearly point to the Li/Ni disorder as the reason $Li(Ni_{0.5}Mn_{0.5})O_2$ has not yet lived up to its high rate potential. The solid lines show the calculated O-O interlayer spacing for a material with 8.3% of Li-Ni site disorder. The dashed lines give the equivalent spacing for a hypothetical material with no Li/Ni disorder. Our calculations indicate that the Li slab space reduces from 2.64 to 2.62 Å when 8.3% of transition metal is present in the Li layer. Li motion is so sensitive to the spacing between oxygen layers that this very small change ($\sim$0.02 Å) results in a 20- to 30-meV increase in the activation barrier. More important, Li/Ni disorder greatly limits the opening of the Li slab space upon delithiation (i.e., on charging the battery). The Li slab space expands during the early stages of delithiation as a result of the removal of O^{2-}-Li^+-O^{2-} bonds across the slab, leading to faster Li motion. Whereas the Li slab space increases from 2.64 to 2.74 Å in a perfect layered system, calculations indicate that it only increases from 2.62 to 2.69 Å when 8.3% Ni ions are present in the Li layer. These observations clearly

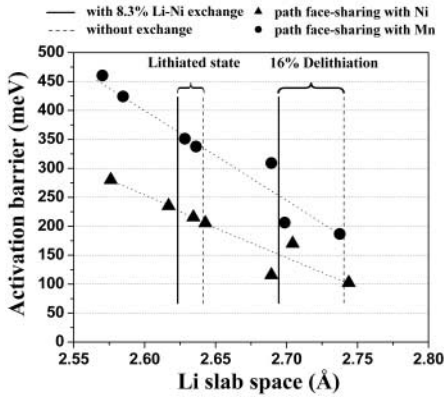

Fig. 2. Calculated activation barrier for Li migration in $Li(Ni_{0.5}Mn_{0.5})O_2$ as a function of the Li slab space. Triangles and circles represent the activated state that face-shares with Ni and Mn, respectively. The activation barriers have been calculated for a hypothetically perfect layered system, for a system with 8.3% excess Ni present in the Li layer without a change in the transition-metal layer, and for a system with 8.3% Li-Ni exchange.

indicate that the diffusivity of Li should be greatly improved by reducing the Li/transition-metal (Ni) exchange in $Li(Ni_{0.5}Mn_{0.5})O_2$, a fact that has already been noticed experimentally in $LiNiO_2$ and $LiTiS_2$ compounds (*11*, *12*).

Although Li-containing materials prepared through traditional high-temperature synthesis routes contain substantial Li/Ni disorder and are, therefore, unlikely to be high-rate electrodes, better ordering can be expected in $Na(Ni_{0.5}Mn_{0.5})O_2$ because the larger size difference between Na^+ and Ni^{2+} or Mn^{4+} creates a larger driving force for separating the alkali ions and the transition-metal ions in discrete layers. We have previously shown that the driving force for layering is likely to be increased if a larger ion, such as Na^+, is used instead of Li^+ because of the increased size mismatch between Na^+ and transition-metal ions such as Ni^{2+} (*13*). Na compounds can be trans-

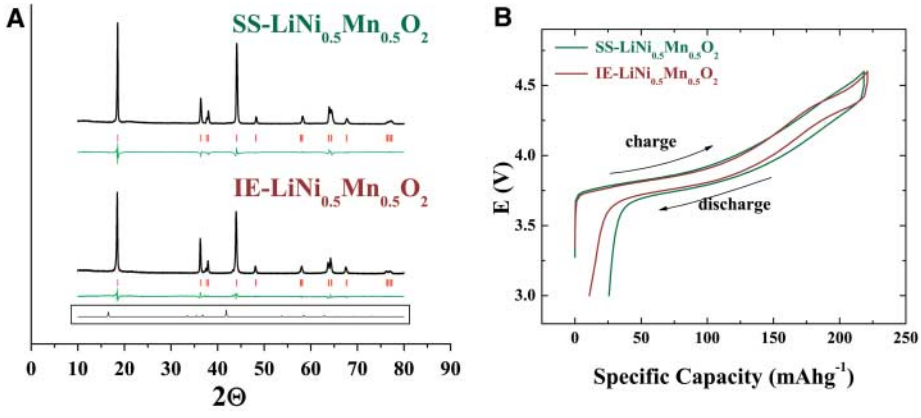

Fig. 3. (**A**) XRD patterns of SS-Li($Ni_{0.5}Mn_{0.5}$)O_2 (top) and IE-Li($Ni_{0.5}Mn_{0.5}$)O_2 (bottom). The observed pattern, the calculated peak positions, and the difference between the two patterns are shown for each XRD pattern. The bottom inset is the XRD pattern of the Na precursor. The precursor peak is not observed after ion exchange. The Rietveld refinement of SS-Li($Ni_{0.5}Mn_{0.5}$)O_2 (in R-3m) gives c = 14.2820(14) Å, a = 2.8850(1) Å, and z = 0.25736(37); the Ni-Li exchange = 10.9%, with R_p = 13.6 and R_{wp} = 15.3. The refinement of IE-Li($Ni_{0.5}Mn_{0.5}$)O_2 gives c = 14.3437(8) Å, a = 2.8924(1) Å, and z = 0.25907(21); the Ni-Li exchange = 4.3%, with R_p = 7.08 and R_{wp} = 8.74. (**B**) First charge/discharge curves of IE-Li($Ni_{0.5}Mn_{0.5}$)O_2 and SS-Li($Ni_{0.5}Mn_{0.5}$)O_2 within the voltage window of 3.0 to 4.6 V at C/20 rate.

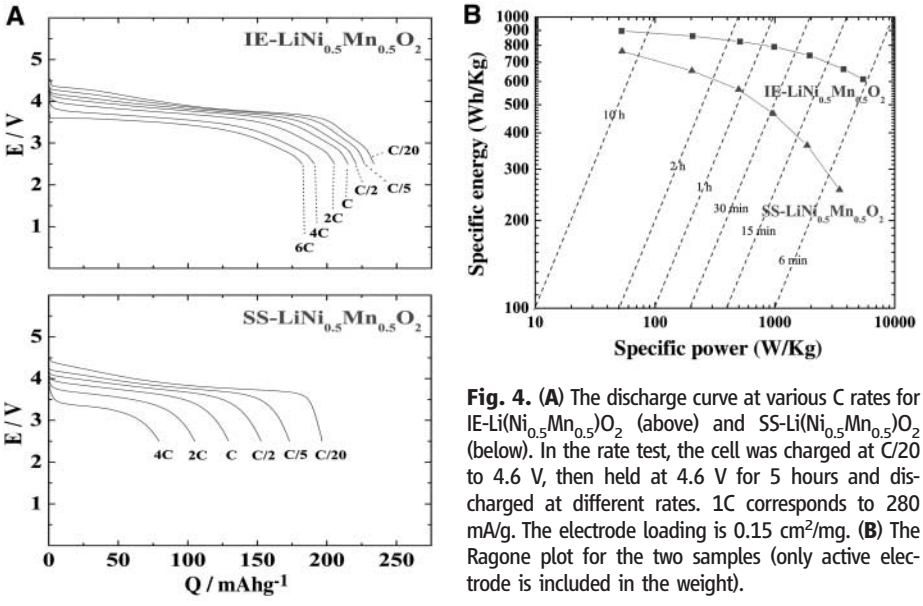

Fig. 4. (**A**) The discharge curve at various C rates for IE-Li($Ni_{0.5}Mn_{0.5}$)O_2 (above) and SS-Li($Ni_{0.5}Mn_{0.5}$)O_2 (below). In the rate test, the cell was charged at C/20 to 4.6 V, then held at 4.6 V for 5 hours and discharged at different rates. 1C corresponds to 280 mA/g. The electrode loading is 0.15 cm^2/mg. (**B**) The Ragone plot for the two samples (only active electrode is included in the weight).

formed to well-layered Li compounds by ion exchange of Na^+ for Li^+ (*14*–*16*). Ion exchange is a soft chemical approach performed at relatively low temperature so that only Na^+ is replaced by Li^+, keeping the rest of the structure intact. We have indeed obtained a well-layered material with excellent performance by ion-exchanging Li for Na in Na($Ni_{0.5}Mn_{0.5}$)O_2. Details of the synthesis procedure are given in the Supporting Online Material (*17*).

The x-ray diffraction (XRD) pattern of the Li($Ni_{0.5}Mn_{0.5}$)O_2 obtained by ion exchange [IE-Li($Ni_{0.5}Mn_{0.5}$)O_2] is shown in Fig. 3A. For comparison, we also show Li($Ni_{0.5}Mn_{0.5}$)O_2 synthesized through a conventional solid-state reaction [SS-Li($Ni_{0.5}Mn_{0.5}$)O_2]. The refined structural parameters for SS-Li($Ni_{0.5}Mn_{0.5}$)O_2 are in good agreement with the literature (*4*, *9*, *10*, *18*–*20*). Noticeably, there is a substantial increase in the c-lattice parameter from 14.28 Å in SS-Li($Ni_{0.5}Mn_{0.5}$)O_2 to 14.34 Å in IE-Li($Ni_{0.5}Mn_{0.5}$)O_2. The c-lattice parameter is perpendicular to the layers in the structure of Fig. 1, and its increase signifies an increase in the space around the Li layer. Defining the Li slab space as the average distance between the oxygen layers around the Li layer, the Li slab space increases from 2.59 Å in SS-Li($Ni_{0.5}Mn_{0.5}$)O_2 to 2.65 Å in IE-Li($Ni_{0.5}Mn_{0.5}$)O_2. Given the computational results in Fig. 2, IE-Li($Ni_{0.5}Mn_{0.5}$)O_2 should therefore have a substantially higher Li diffusivity. The small quantitative disagreement with the calculated slab spaces is typical for modern ab initio approaches. No Na precursor peaks are visible in the XRD, and only about 0.3 weight percent of Na could be detected by inductively coupled plasma (ICP) measurement in IE-Li($Ni_{0.5}Mn_{0.5}$)O_2, which implies that the ion exchange of Na and Li is complete.

Rietveld refinement of the XRD gives Li/Ni exchanges of 10.9% and 4.3%, respectively, in the SS-Li($Ni_{0.5}Mn_{0.5}$)O_2 and IE-Li($Ni_{0.5}Mn_{0.5}$)O_2. Because the site occupancies obtained by Rietveld refinement can be somewhat inaccurate as a result of preferential texture of the sample, and when refining occupancies for multiple cations on the same crystallographic site, the Li/Ni exchange was independently verified by solid state ^{6}Li magic angle spinning nuclear magnetic resonance (MAS NMR). Quantitative analysis of the 1450–parts per million peak in the NMR spectrum, which is known to correspond to Li in a transition-metal site (*21*), reveals that Li-Ni exchange is even lower, about 0.5% (*17*). This suggests that our strategy to obtain a better layered structure with larger slab space is successful.

Electron microscopy revealed plate-shaped crystals of about 1 μm for IE-Li($Ni_{0.5}Mn_{0.5}$)O_2, whereas the SS-Li($Ni_{0.5}Mn_{0.5}$)O_2 forms cubic particles of about 0.5 μm (*17*). The anisotropic shape of the crystallites offers further evidence for the more layered structure of IE-Li($Ni_{0.5}Mn_{0.5}$)O_2.

Figure 3B shows the first charge and discharge profiles of IE-Li($Ni_{0.5}Mn_{0.5}$)O_2 and SS-Li($Ni_{0.5}Mn_{0.5}$)O_2 tested in an electrochemical cell at a rate corresponding to fully charging the theoretical capacity of the material in 20 hours (C/20). Whereas the charge/discharge behavior of IE-Li($Ni_{0.5}Mn_{0.5}$)O_2 is very similar to that of SS-Li($Ni_{0.5}Mn_{0.5}$)O_2 below 4 V, the plateau at 4.3 V is more pronounced in IE-Li($Ni_{0.5}Mn_{0.5}$)O_2. Because the 4.3-V plateau is observed at about x = 0.6 to 0.7 [Li_{1-x}($Ni_{0.5}Mn_{0.5}$)O_2], it could be caused by Li-vacancy ordering (*22*). The absence of transition metals in the Li layer is likely to enhance Li-vacancy ordering.

Figure 4A shows that, despite its larger particle size, the rate capability of IE-Li($Ni_{0.5}Mn_{0.5}$)O_2 is superior to that of SS-Li($Ni_{0.5}Mn_{0.5}$)O_2. Although the performance of the materials is similar at low rates, IE-Li($Ni_{0.5}Mn_{0.5}$)O_2 retains much higher capacity at high rates than does SS-Li($Ni_{0.5}Mn_{0.5}$)O_2. Even at a 6C rate (one charge of 280 mAh/g in 10 min), IE-Li($Ni_{0.5}Mn_{0.5}$)O_2 delivers a discharge capacity of 183 mAh/g. There is no published data available for a rate as high as 6C, but comparison with the best electrochemical data published for this material so far [135 mAh/g at a 397 mA/g rate (*9*)] confirms that we have developed a material with substantially improved performance.

For practical applications, the trade-off between power (rate) and energy density is important and is often represented in a Ragone plot (Fig. 4B). Most Li-battery materials show a substantial decrease in specific energy as one draws more current from them, making them less useful in applications such as EV (electric vehicle), HEV, and power tools, where high charge and

discharge rates are required. Figure 4B shows that IE-Li($Ni_{0.5}Mn_{0.5}$)O_2 clearly retains its energy storage capacity even at the very high rate required for those applications. At a 6-min charge/discharge rate, IE-Li($Ni_{0.5}Mn_{0.5}$)O_2 delivers almost double the energy density of SS-Li($Ni_{0.5}Mn_{0.5}$)O_2. Initial tests on the capacity retention with full charge/discharge cycling are promising, with a fade of 0.6% per cycle for IE-Li($Ni_{0.5}Mn_{0.5}$)O_2 versus 0.8% per cycle for SS-Li($Ni_{0.5}Mn_{0.5}$)O_2 (*17*).

In conclusion, we have used ab initio computational modeling to infer that the combined use of low-valent transition-metal cations and low strain in the activated state are key strategies for increasing the rate capability of layered cathode materials, and we have successfully synthesized Li($Ni_{0.5}Mn_{0.5}$)O_2 with very little intralayer disordering to optimize those factors. In agreement with our theoretical predictions, this material retains its capacity at high rates. Substitution of Co for Ni and Mn can also be used to reduce the Li/Ni exchange and improve rate performance (*23*, *24*), although the use of Co increases the cost and reduces the safety of the material (*25*). Although Li($Ni_{0.5}Mn_{0.5}$)O_2 displays an exciting combination of high rate and high capacity, several other factors, such as thermal stability, cycle life, and the extra cost from the ion-exchange process, will need to be further investigated before its application in commercial products can be considered. If the outcome of such development studies is positive, Li($Ni_{0.5}Mn_{0.5}$)O_2 would be a potential cathode material for high rate applications.

References and Notes

1. M. S. Whittingham, *Science* **192**, 1126 (1976).
2. A. Van der Ven, G. Ceder, *Electrochem. Solid-State Lett.* **3**, 301 (2000).
3. A. Van der Ven, G. Ceder, *J. Power Sources* **97-98**, 529 (2001).
4. T. Ohzuku, Y. Makimura, *Chem. Lett. (Jpn.)* **8**, 744 (2001).
5. Z. Lu, D. D. MacNeil, J. R. Dahn, *Electrochem. Solid-State Lett.* **4**, A191 (2001).
6. J. Reed, G. Ceder, *Electrochem. Solid-State Lett.* **5**, A145 (2002).
7. J. M. Paulsen, J. R. Dahn, *J. Electrochem. Soc.* **147**, 2478 (2000).
8. M. M. Thackeray, *Prog. Solid State Chem.* **25**, 1 (1997).
9. Y. Makimura, T. Ohzuku, *J. Power Sources* **119-121**, 156 (2003).
10. Z. Lu, L. Y. Beaulieu, R. A. Donaberger, C. L. Thomas, J. R. Dahn, *J. Electrochem. Soc.* **149**, A778 (2002).
11. C. Delmas *et al.*, *J. Power Sources* **68**, 120 (1997).
12. M. S. Whittingham, U.S. Pat. 4,007,055 (1975).
13. E. J. Wu, P. D. Tepesch, G. Ceder, *Philos. Mag. B* **77**, 1039 (1998).
14. A. R. Armstrong, P. G. Bruce, *Nature* **381**, 499 (1996).
15. C. Delmas, J. J. Braconnier, A. Maazaz, P. Hagenmuleer, *Rev. Chimie Minérale* **19**, 343 (1982).
16. K. Kang *et al.*, *Chem. Mater.* **15**, 4503 (2003).
17. Materials and methods are available as supporting material on *Science* Online.
18. Y. S. Meng *et al.*, *Chem. Mater.* **17**, 2386 (2005).
19. H. Kobayashi *et al.*, *J. Mater. Chem.* **13**, 590 (2003).
20. W. S. Yoon *et al.*, *Electrochem. Solid-State Lett.* **5**, A263 (2002).
21. C. P. Grey, W. S. Yoon, J. Reed, G. Ceder, *Electrochem. Solid-State Lett.* **7**, A290 (2004).
22. C. Delmas *et al.*, *Int. J. Inorg. Mater.* **1**, 11 (1999).
23. Z. Lu, D. D. MacNeil, J. R. Dahn, *Electrochem. Solid-State Lett.* **4**, A200 (2001).
24. T. Ohzuku, Y. Makimura, *Chem. Lett. (Jpn.)* **7**, 642 (2001).
25. J. Jiang, K. W. Eberman, L. J. Krause, J. R. Dahn, *J. Electrochem. Soc.* **152**, A1879 (2005).

26. The authors would like to thank Y. Shao-Horn for valuable discussion. This work was supported by the Materials Research Science and Engineering Centers program of the National Science Foundation under award DMR 02-13282 and by the Assistant Secretary for Energy Efficiency and Renewable Energy, Office of FreedomCAR and Vehicle Technologies of the U.S. Department of Energy under contract DE-AC03-76SF00098, subcontracts 6517748 and 6517749, with the Lawrence Berkeley National Laboratory.

Supporting Online Material

www.sciencemag.org/cgi/content/full/311/5763/977/DC1
Materials and Methods
Figs. S1 to S4
References

2 November 2005; accepted 20 January 2006
10.1126/science.1122152

Plasma Acceleration Above Martian Magnetic Anomalies

R. Lundin,[1] D. Winningham,[2] S. Barabash,[1] R. Frahm,[2] M. Holmström,[1] J.-A. Sauvaud,[3] A. Fedorov,[3] K. Asamura,[4] A. J. Coates,[5] Y. Soobiah,[5] K. C. Hsieh,[6] M. Grande,[7] H. Koskinen,[8,9] E. Kallio,[8] J. Kozyra,[10] J. Woch,[11] M. Fraenz,[11] D. Brain,[12] J. Luhmann,[12] S. McKenna-Lawler,[13] R. S. Orsini,[14] P. Brandt,[15] P. Wurz[16]

Auroras are caused by accelerated charged particles precipitating along magnetic field lines into a planetary atmosphere, the auroral brightness being roughly proportional to the precipitating particle energy flux. The Analyzer of Space Plasma and Energetic Atoms experiment on the Mars Express spacecraft has made a detailed study of acceleration processes on the nightside of Mars. We observed accelerated electrons and ions in the deep nightside high-altitude region of Mars that map geographically to interface/cleft regions associated with martian crustal magnetization regions. By integrating electron and ion acceleration energy down to the upper atmosphere, we saw energy fluxes in the range of 1 to 50 milliwatts per square meter per second. These conditions are similar to those producing bright discrete auroras above Earth. Discrete auroras at Mars are therefore expected to be associated with plasma acceleration in diverging magnetic flux tubes above crustal magnetization regions, the auroras being distributed geographically in a complex pattern by the many multipole magnetic field lines extending into space.

Earth's polar aurora and related phenomena, such as magnetic and ionospheric disturbances, have been studied for well over half a century. The first proof that the aurora is caused by energetic electrons precipitating into Earth's topside atmosphere came from high-altitude sounding-rocket measurements (*1*). Electrons accelerated downward by magnetic field–aligned electric fields cause intense bright auroral arcs, often referred to as discrete auroras. Intense fluxes of nearly monoenergetic electrons (*2*) were the first evidence for magnetic field–aligned electric fields. Subsequent observations of accelerated electrons were made from polar orbiting satellites. The electrons' peak energy displayed a characteristic "inverted-V" signature in an energy-time spectrogram (*3*), which became the particle attribute of a discrete aurora. An additional proof of concept was observations of electrons and ions accelerated in opposite directions (*4*, *5*).

Inverted-V–like ion features near Mars, first reported by the Phobos-2 spacecraft (*6*), were associated with the temporal and spatial variability of the energy and momentum transfer between martian plasma and the solar wind (*7*, *8*). This was because auroras, specifically discrete auroras, are associated with magnetized planets, and no strong intrinsic magnetic fields were evident from Phobos-2 data, thus ruling out any analogy with the terrestrial aurora.

The Mars Global Surveyor (MGS) findings of crustal magnetic anomalies at Mars (*9*) considerably changed the picture. We now expect to find diverging magnetic field "cusps" above Mars (*10*) and closed magnetic loops (*11*), with local magnetic conditions similar to those found above Earth's polar region, albeit weaker and topologically different. A set of magnetic multipoles at specific longitudes and latitudes of Mars may characterize the crustal magnetization. Indeed, the first observation of auroral emission at Mars (*12*) was made above a strong crustal magnetization at 177°E and 52°S. The emissions in the 150- to 300-nm bands (CO and O) were most likely excited by high fluxes of charged particles.

Our study identified regions with downward-accelerated electrons and upward-accelerated ionospheric ions near local midnight. We studied how the acceleration regions map to magnetic cusps and clefts bound by strong magnetizations at Mars. We compared the energy spectra of accelerated electrons in the nightside of Mars with those associated with terrestrial discrete auroras. Finally, we computed the energy flux of precipitating electrons and estimated, from a